Continuous Phase Denoising via Deep Learning Based on Perlin Noise Similarity in Digital Holographic Microscopy

Jianjun Tang, Benyong Chen, Liping Yan, and Liu Huang

***Abstract*—Deep learning (DL), as a powerful tool for image processing by learning from data, brings significant advantages for solving the noise in phase images of digital holography. However, due to the inaccurate representation of the features of the actual digital holographic hybrid phase noise (DHHPN), most DL-based denoising strategies that use a Gaussian noise model to generate simulated datasets for training have unsatisfactory performance. Here, to explore the characteristics of actual DHHPN, we evaluate the correlations between the DHHPN obtained from different DH/DHM experiments and five types of noise (Uniform, Normal, Pink, Brown and Perlin) in terms of maximum information coefficient and Pearson correlation coefficient. For the first time, to the best of our knowledge, we have revealed an extremely high similarity between DHHPN and Perlin noise. Based on this discovery, a continuous phase denoising method via deep learning based on Perlin noise similarity is proposed. Without needing to collect and label experimental training data at high cost, a dataset consisting only of computer-generated clean sample images and Perlin noise images can be easily obtained. This simulated dataset is then used to train our designed convolutional neural network. Simulation and experimental results show that the denoising performance of the proposed method far exceeds the other two classical methods, and the standard deviation of the measurement results is reduced by an order of magnitude, reaching the sub-nanometer level. The proposed method has significant application in the fields of digital holographic precision measurements.**

***Index Terms*—Deep learning (DL), digital holography (DH), microstructure measurement, phase denoising.**

Manuscript received 8 September 2023; revised 11 January 2024; accepted 20 February 2024. Date of publication 22 March 2024; date of current version 5 June 2024. This work was supported by the National Natural Science Foundation of China under Grant 52035015. Paper no. TII-23-3438. *(Corresponding author: Liping Yan.)*

Jianjun Tang is with the Laboratory for Laser Precision Measurement, School of Mechanical Engineering, Zhejiang Sci-Tech University, Hangzhou 310018, China (e-mail: jianjtang@mails.zstu.edu.cn).

Benyong Chen, Liping Yan, and Liu Huang are with the Laboratory for Laser Precision Measurement, School of Information Science and Engineering, Zhejiang Sci-Tech University, Hangzhou 310018, China (e-mail: chenby@zstu.edu.cn; yanliping@zstu.edu.cn; huangliu@zstu.edu.cn).

Color versions of one or more figures in this article are available at https://doi.org/10.1109/TII.2024.3375375.

Digital Object Identifier 10.1109/TII.2024.3375375

I. Introduction

DIGITAL holography (DH) interferometry, with the advantages of noncontact, high sensitivity, and real-time quantitative phase measurements (QPM), has been widely applied in microfluidic imaging, live cell detection, microelectro mechanical system (MEMS) measurements, and other fields. However, due to the characteristics of the image recording sensor, the diffuse reflection and scattering of the sample surfaces, kinds of noises, such as photon noise, electronic noise, quantum noise, and speckle noise, are introduced into the recorded digital interferograms [1]. These noises with different features are superimposed on the sample phase, seriously affecting the measurement accuracy.

Currently, numerical denoising algorithms have been widely studied and can generally be categorized into three types: 1) spatial domain-based methods [2], [3], [4], [5]; 2) transform domain-based methods [6], [7], [8] and 3) learning-based methods [9], [10], [11], [12], [13], [14], [15], [16], [17]. With the development of deep learning (DL), an increasing number of DL-based denoising methods are applied to QPM, demonstrating robust denoising performance. However, acquiring large and effective datasets remains a significant challenge for these DL-based denoising algorithms. First, collecting a substantial amount of experimental training data is a labor-intensive task. Currently, no universal denoising algorithm can completely suppress real noise and provide clean learning labels for training [1]. Second, for computationally generated datasets, no model has been demonstrated that can accurately characterize the real experimental noise [18]. Presently, most DL-based denoising methods use a Gaussian noise model to create datasets for training convolutional neural networks (CNN) to reduce speckle noise in wrapped phase maps. For instance, two CNN-based methods [9] and [10] achieved denoising performance comparable to 2-D windowed Fourier transform filtering (WFT2F). WFT2F is a popular and powerful high-frequency speckle noise suppression algorithm, but it requires high computational costs and experience in parameter tuning, and residual nonspeckle noise still remains in the phase maps after filtering.

Fig. 1 illustrates the denoising performance of WFT2F and DnCNN [19] on experimental data from digital holographic microscopy (DHM) and simulated Gaussian noise phase data. Initially, datasets of wrapped phase (including real and imaginary parts) and continuous phase with added Gaussian noise

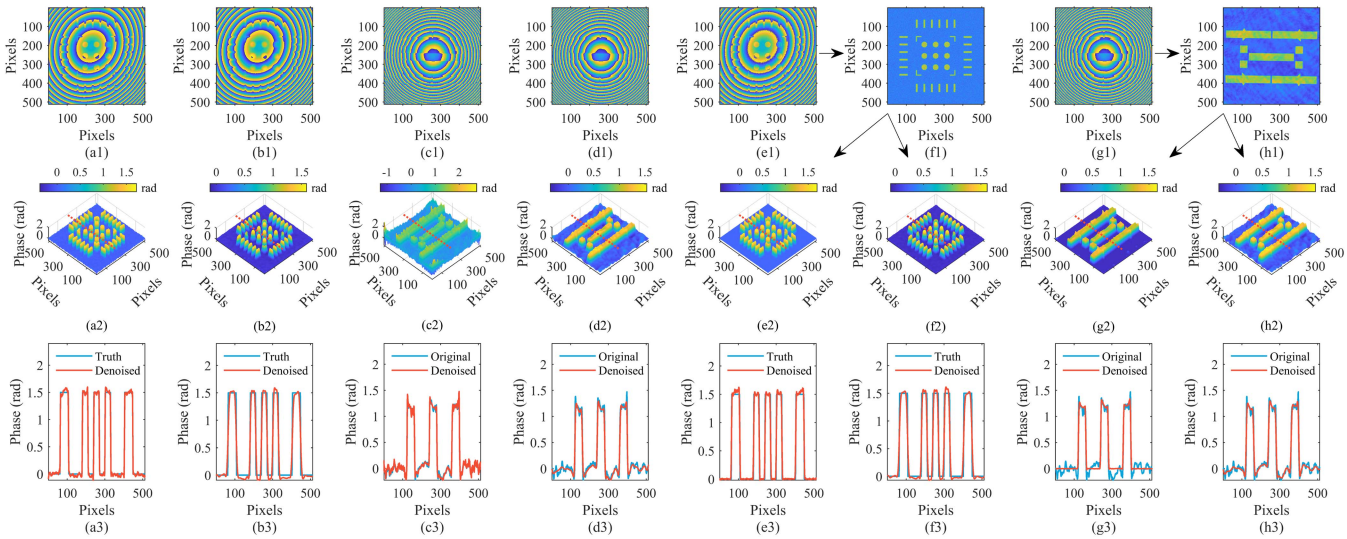

Fig. 1. Denoising performance of WFT2F and DnCNN. Columns 1, 2, 5, and 6: Simulation data with added Gaussian noise. Columns 3, 4, 7, and 8: Experimental data from the DHM system. (a1) and (c1) Denoised wrapped phase maps obtained by DnCNN trained on simulation data with added Gaussian noise for the real and imaginary parts. (b1) and (d1) Denoised wrapped phase maps obtained by WFT2F. (e1) and (g1) Original wrapped phase maps without denoising. (f1) and (h1) Continuous phase maps obtained by phase unwrapping and aberration compensation from (e1) and (g1), respectively. (a2)–(d2) Continuous phase maps obtained by phase unwrapping and aberration compensation from (a1)–(d1). (e2) and (g2) Denoising results obtained by DnCNN trained on continuous phase data with added Gaussian noise for (f1) and (h1), respectively. (f2) and (h2) Denoising results by WFT2F for (f1) and (h1), respectively. (a3)–(h3) Profiles at the red dashed lines in (a2)–(h2).

were generated. DnCNN was then separately trained to denoise different forms of phase maps. From the simulation data in Fig. 1(a2), (b2), (e2), and (f2) and their corresponding profiles in Fig. 1(a3), (b3), (e3), and (f3), it can be seen that the denoising effect is quite good no matter the WFT2F or DnCNN method is used, and no matter the denoising is performed on the wrapped phase maps or continuous phase maps. From the experiment data in Fig. 1(d2) and (h2) and their corresponding profiles in Fig. 1(d3) and (h3), the denoising effect of WFT2F for wrapped phase maps and continuous phase maps are nearly identical. Obviously, it can be seen from Fig. 1(h1) and (h3) (blue line) that the original continuous phase of sample includes not only high-frequency speckles, but also low-frequency fluctuations. This shows that the noises introduced into DH is a kind of hybrid noise with a wide spectrum, which we define as digital holographic hybrid phase noise (DHHPN). In addition, from the red lines in Fig. 1(d3) and (h3), whether WFT2F is performed before or after phase unwrapping, only high-frequency speckle noise can be suppressed, resulting in residual wave-like noise in the phase result, which affects the measurement accuracy. From the experiment data in Fig. 1(c2) and (g2) and their corresponding profiles in Fig. 1(c3) and (g3), the denoising effect of DnCNN for continuous phase map is better than its denoising effect for wrapped phase map. Although the denoising effect of DnCNN on the wrapped phase map appears similar to that of WFT2F, there is still significant noise present in the recovered sample phase. Compared to WFT2F, although DnCNN achieves relatively good suppression of background noise in the denoised result of continuous phase map (this may be attributed to the generalization ability of neural networks), noise in the sample region is hardly removed, which still affects the measurement accuracy. According to previous study [20], the point spread function of digital holographic imaging systems will make the noise in the phase data not follow Gaussian statistics. Therefore, for CNN-based DH denoising algorithms, generating a training dataset by simulating the noise with a single Gaussian model has limited denoising effect for such DHHPN. In addition, the wrapped phase maps of DHM usually contain a large amount of phase aberrations, obscuring the low-frequency noise. Wrapped phase maps with aberrations make it challenging for CNN to extract comprehensive features of low-frequency noise, resulting in limited denoising performance.

In this article, continuous phase denoising via deep learning based on Perlin noise similarity in DHM is proposed. The correlations between the DHHPN obtained from different DH/DHM experiments and five types of noise (Uniform, Normal, Pink, Brown, and Perlin (UNPBP) [21] in terms of maximum information coefficient and Pearson correlation coefficient, and the characteristic similarity between DHHPN and Perlin noise is revealed. Inspired by this research, Perlin noise is employed to simulate the real DHHPN, and a CNN trained solely on the simulated Perlin dataset achieves effective denoising of DHHPN. The following sections will introduce the principles of the proposed method, the implementation of CNN training, simulation validation, and measurement experiments on two different samples.

II. Principle and Realization

A. Characteristics Analysis of Noise

First, to study the characteristics of real DHHPN, the background region in continuous phase map of a USAF1951 positive resolution target obtained from DHM system was analyzed and

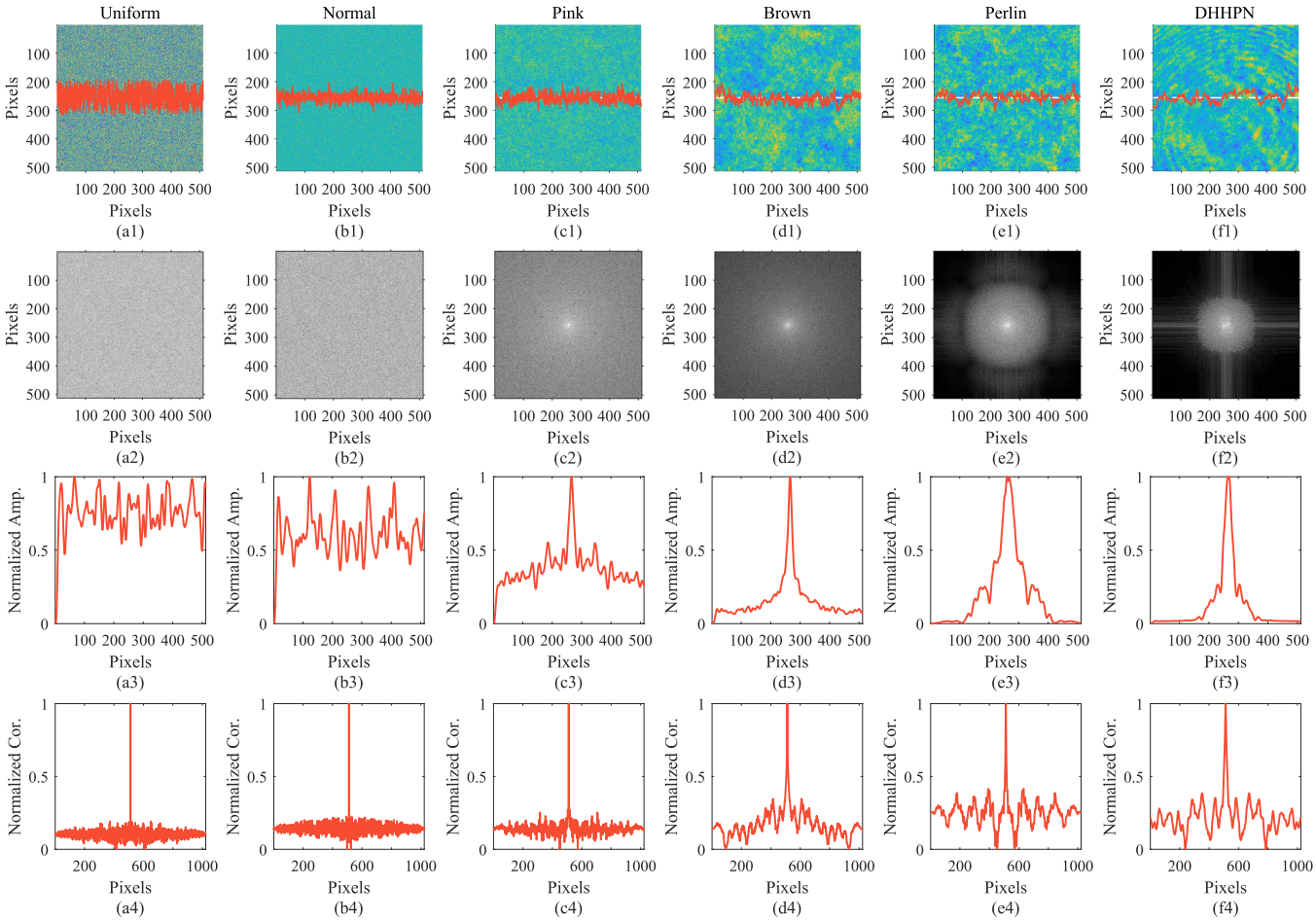

Fig. 2. Characteristic analysis and comparison of DHHPN and UNPBP. (a1)–(f1) Noise images of Uniform, Normal, Pink, Brown, Perlin, and DHHPN. (a2)–(f2) 2-D Fourier spectra amplitudes of (a1)–(f1). (a3)–(f3) Normalized amplitudes of 1-D Fourier spectra of the 256th row data in (a1)–(f1). (a4)–(f4) Normalized values of autocorrelation functions of the 256th row data in (a1)–(f1).

compared with UNPBP. As shown in Fig. 2, Uniform and Normal were generated using the "rand" and "randn" functions in MATLAB, respectively. Pink and Brown were generated using the method from [22], setting the spectral density factor β to –1 and –2, respectively. Perlin was generated according to the method in [23]. The width and height of all noise images in Fig. 2(a1)–(f1) are 512 pixels, with an average value of 0 rad and a standard deviation of 0.13 rad. The red curve plots the data distribution of the 256th row of each noise image.

From the 2-D Fourier spectra in Fig. 2(a2)–(f2), the frequency components of Uniform and Normal are relatively uniformly distributed, whereas the frequency components of Pink, Brown, Perlin, and DHHPN are dominated by low frequencies (located at the center of the Fourier spectrum), and the high-frequency components gradually decrease. Furthermore, the normalized amplitude of the 1-D Fourier spectra in Fig. 2(a3)–(f3) show that the amplitudes of Uniform and Normal fluctuate around a certain value in the whole frequency domain, with average values of 0.75 and 0.60, respectively. All the amplitudes of Pink, Brown, Perlin, and DHHPN exhibit a main peak near zero frequency, with Pink and Brown containing more high-frequency components, fluctuating around values of 0.40 and 0.10, respectively. Clearly, Perlin and DHHPN have relatively fewer high-frequency components and exhibit a similar decreasing trend. In addition, the autocorrelation functions were also calculated and compared [24]. As shown in Fig. 2(a4)–(f4), Uniform, Normal, and Pink have almost no autocorrelation, whereas Brown, Perlin, and DHHPN exhibit noticeable autocorrelation, indicating noncompletely random signals. Among them, the autocorrelation functions of DHHPN and Perlin are the most similar. Therefore, from the comparisons of noise distributions, spectra, and autocorrelation functions, it can be intuitively observed that the characteristics of DHHPN and Perlin are highly similar.

To more accurately demonstrate the highest similarity between DHHPN and Perlin, we separately calculated the Pearson correlation coefficients (Pearson's r) [25] for the spectra and autocorrelation functions of DHHPN relative to UNPBP. Pearson's r describes the strength and direction of the linear relationship between two quantitative variables, which can be used to test whether a significant relationship exists between two variables. The formula for calculating Pearson's r is

$$r(X,Y) = \frac{1}{N-1}\sum_{i=1}^{N}\left(\frac{X_i-\overline{X}}{\sigma_X}\right)\left(\frac{Y_i-\overline{Y}}{\sigma_Y}\right) \quad (1)$$

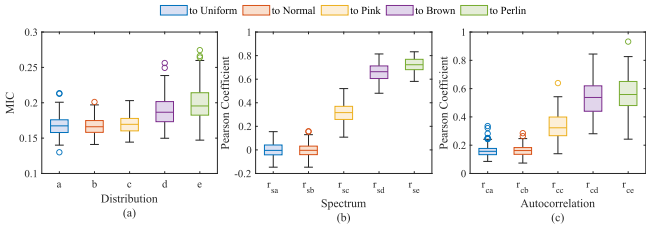

Fig. 3. Statistical analysis of feature similarity of DHHPN relative to UNPBP. (a) MIC for the distribution of noise data. (b) and (c) Pearson's r for the spectra and autocorrelation functions, respectively.

where X and Y represent two different datasets, N denotes the data sizes, $\overline{X}$ and $\overline{Y}$ denote the means of X and Y, and σ_X and σ_Y represent the standard deviation of X and Y, respectively. The Pearson's r is a numeric value ranging from –1 to 1. The correlations are defined as strong when $0.5 \leq r \leq 1.0$ or $-1.0 \leq r \leq -0.5$, moderate when $0.3 \leq r < 0.5$ or $-0.5 < r \leq -0.3$, and weak or no correlation when $-0.3 < r < 0.3$.

We also evaluate the similarity of the distribution characteristics of DHHPN relative to UNPBP. As Pearson's r can only calculate linear relationships and is highly sensitive to noise, it cannot directly explore the relationships between noise distributions. Therefore, we employed the more robust maximum information coefficient (MIC) [26] to study the correlation between noise distributions. MIC is a nonparametric exploration of maximum information, calculating the linear or nonlinear correlation between two random variables. The MIC is calculated using the formula

$$I(X,Y) = \sum_{y\in Y}\sum_{x\in X} p(x,y)\log_2\frac{p(x,y)}{p(x)p(y)}$$
$$\mathrm{MIC}(X,Y) = \max_{|X||Y|<B}\frac{I(X,Y)}{\log_2\min(|X|,|Y|)} \tag{2}$$

where I represents the mutual information of random variables X and Y, $p(x,y)$ is the joint probability mass function of X and Y, and $p(x)$ and $p(y)$ are the marginal probability mass functions of X and Y, respectively. B is typically 0.6 power of the data size N.

By randomly selecting 64 rows of data and 64 columns of data from the DHHPN image in Fig. 2(f1), we create a dataset $X_{512\times128}$, comprising 128 vectors. Similarly, we obtain five different datasets $Y_{k,512\times128}$ (for $k = a, b, c, d, e$) from the UNPBP images in Fig. 2(a1)–(e1). For each pair (X, Y_k), we calculate the MIC with (2) and obtain 128 coefficients. Fig. 3(a) shows the boxplot of MIC for DHHPN relative to UNPBP. Compared to the other four types of noise, DHHPN is closer to Perlin in terms of noise distributions. Likewise, for each pair (X, Y_k), the 1-D Fourier spectra and autocorrelation functions are first calculated. Then, the spectra Pearson's r (r_{sk}) and autocorrelation functions Pearson's r (r_{ck}) are calculated with (1) and two sets of 128 coefficients are obtained for each kind of UNPBP images. Fig. 3(b) and (c) show boxplots of Pearson's r of spectra and autocorrelation functions for DHHPN relative to UNPBP. It can be seen that, both the correlations between DHHPN and Perlin and between DHHPN and Brown are strong, with median r_{se} and median r_{ce} being 0.72 and 0.56, and median r_{sd} and median r_{cd} being 0.66 and 0.54, respectively. However, DHHPN is more correlated with Perlin. As for Uniform, Normal, and Pink, the median Pearson's r values of spectra and autocorrelation functions are below 0.32 and 0.33, respectively.

From the above analysis, it can be seen that DHHPN exhibits the highest feature similarity with Perlin, which means that Perlin noise can simulate the characteristics of DHPN to a certain extent and provide a reliable noise model for subsequent digital holographic denoising methods.

To further investigate the feature similarity between DHHPN and Perlin in real sample measurements, we extracted data from the background regions of six original phase maps corresponding to four different samples without any denoising for analysis. In the first row of Fig. 4, from left to right, the phase maps correspond to: Reflective coaxial DHM measuring standard microstructure; reflective off-axis DHM measuring standard microstructure; reflective off-axis DHM measuring USAF1951 positive resolution target; transmissive off-axis DH measuring USAF1951 negative resolution target; transmissive off-axis DH measuring roughness sample; and transmissive coaxial DH measuring roughness sample. The illumination light source for the first image is a femtosecond laser with a wavelength of 780 nm, and the others are illuminated with a frequency-stabilized He-Ne laser with a wavelength of 633 nm. The standard microstructure is made of silicon, and the positive/negative resolution targets are made of chrome-on-glass, and the roughness sample are made of glass with grooved structures. The image sensors used for recording holograms in the second to fourth experiments are Basler acA2040-90 m, and the other three experiments use another image sensor HIKROBOT MV-CA016-10UM.

In Fig. 4, for each phase maps, the phase data along the horizontal (red) and vertical (green) dashed lines are extracted to generate $X_{n,512\times2}$ (for $n = 1, 2, \ldots, 6$). The characteristics of phase noise are analyzed by calculating the MIC of the data distribution, as well as the Pearson's r for the spectra and autocorrelation functions. Each set of data along the dashed lines is paired with the aforementioned Y_k and the MIC and Pearson's r calculations are performed for each vector in Y_k. In other words, each dashed background data obtains 128 coefficients, and each experimental image obtains 256 coefficients for each noise type Y_k.

It can be seen from Fig. 4 that no matter what illumination light is adopted, what DH/DHM systems are adopted, what image sensors are used, and what samples are measured, the noise characteristics of the phase maps obtained in DH/DHM systems are surprisingly similar to that of Perlin noise. In the experiments, all the median values of MIC and Pearson's r relative to Perlin for DHHPN are the highest, and all the median values of Pearson's r exceeding 0.50. From the experimental analysis results, it can be seen that there is a strong similarity between the features of DHHPN and Perlin. Therefore, in this article, Perlin noise model is used to generate phase noise to simulate the DHHPN. Combining with the phase maps of different sample randomly generated by simulation, a simulated dataset can be easily obtained to train the CNN designed for denoising continuous phase maps of DH/DHM.

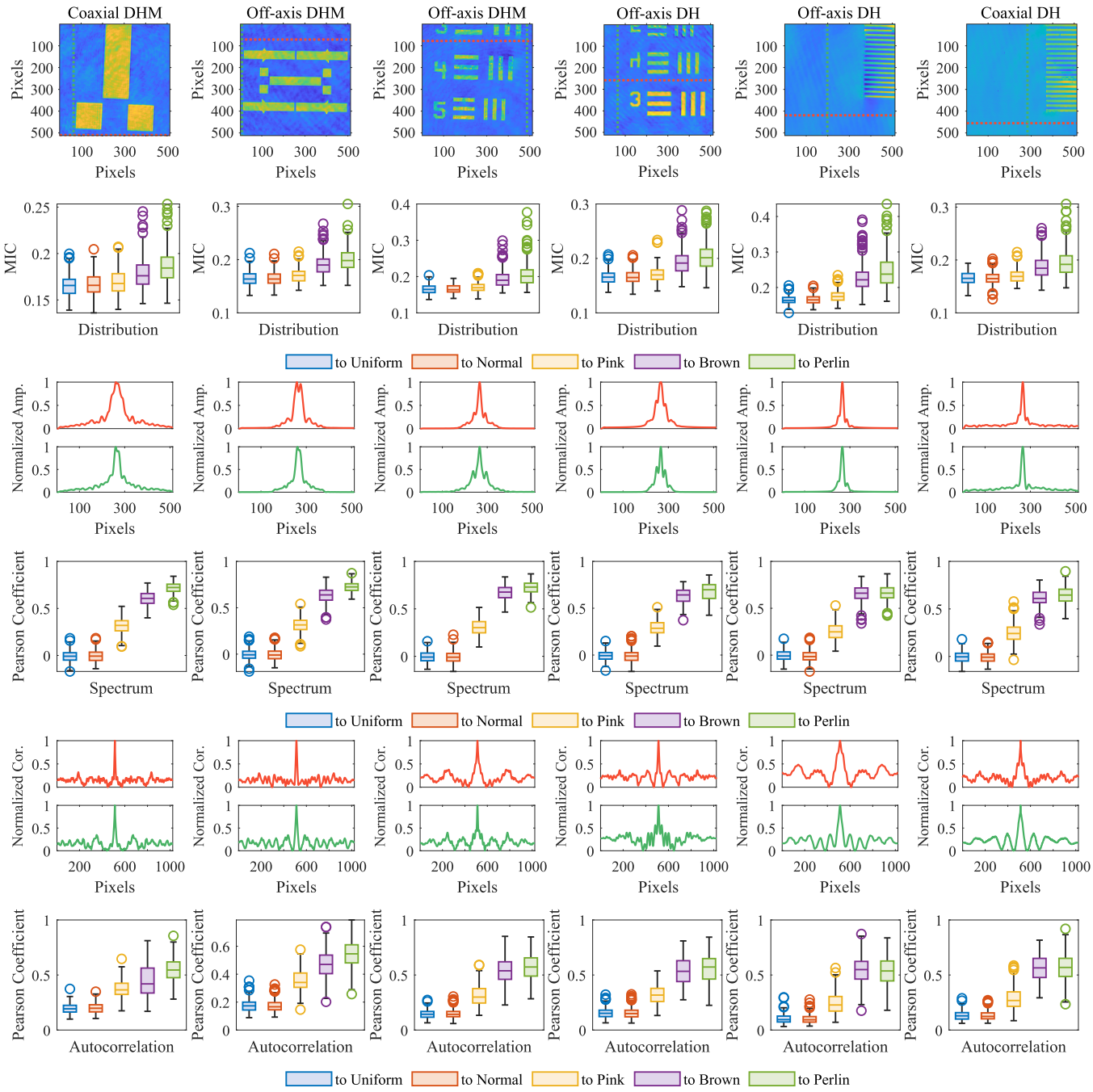

Fig. 4. Feature analysis and comparison of DHHPN in phase maps from four samples obtained with different DH/DHM systems. Row 1 shows the phase maps obtained from the six experiments. Row 2 displays the MIC of the dashed regions relative to UNPBP. Row 3 presents the normalized amplitude of the 1-D Fourier spectra of the dashed regions. Row 4 shows the spectra Pearson's r of the dashed regions relative to UNPBP. Row 5 displays the normalized value of the autocorrelation functions of the dashed regions. Row 6 presents the autocorrelation functions Pearson's r of the dashed regions relative to UNPBP.

B. Design of CNN and Dataset Generation

Generally, after aberration compensation, the phase map obtained by the DH/DHM systems can be expressed as follows:

$$\varphi = \varphi_{\text{sample}} + \varphi_{\text{noise}} \tag{3}$$

where φ_{sample} and φ_{noise} represent the sample phase and noise phase, respectively. CNN-based denoising methods essentially separate the sample phase from the deformed phase and output the former. The mapping relationship between the input and output of CNN can be expressed as $\varphi_{\text{sample}} = \text{CNN}(\varphi)$. DnCNN has the advantages such as fewer parameters and lower computational costs, but its performance is limited when fitting highly complex DHHPN datasets. Therefore, in this article, an end-to-end CNN structure is designed based on DnCNN. By introducing dilation convolutional layers, residual connections, and subspace attention mechanism, the network is more effectively

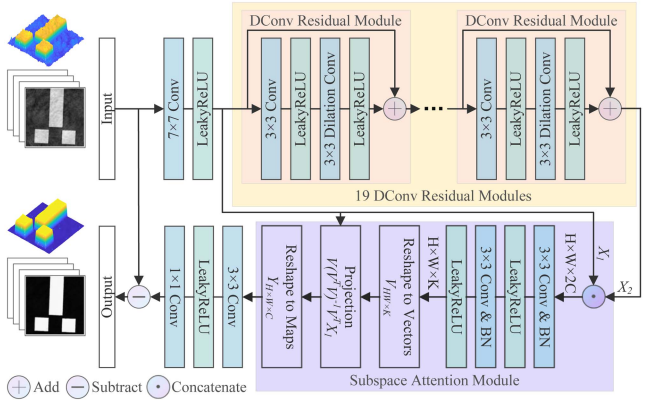

Fig. 5. CNN structure of the proposed method.

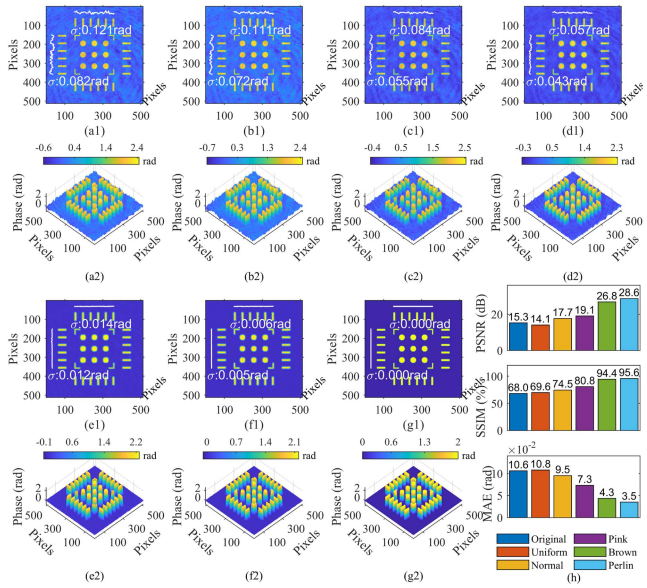

Fig. 6. Simulation evaluation of the proposed method. (a1) Original 2-D phase map obtained by adding the DHHPN shown in Fig. 2(f1) to the ideal sample phase shown in (g1). (b1)–(f1) 2-D phase maps after denoising using the proposed CNN trained on the UNPBP datasets, respectively. (g1) Simulated ideal sample phase map. (a2)–(g2) 3-D phase distributions corresponding to (a1)–(g1). (h) Evaluation of PSNR, SSIM, and MAE for the phase maps before and after denoising.

to fit DHHPN datasets. Due to the autocorrelation in DHHPN, the continuous features span a larger pixel range, requiring a network with an expanded receptive field to effectively extract these features. To address this requirement, we employ larger convolutional kernels in the input layer and incorporate dilation convolutional layers in the hidden layers to enhance the network's receptive field. Given the intricate nature of the noise, the network requires deeper convolutional layers for proper fitting of the dataset. To improve stability and accelerate the training procedure, we introduce residual connections. The attention mechanism primarily utilizes the subspace projection method of algebraic calculations. This mechanism projects feature maps of different dimensions extracted by the network, facilitating the separation of noise components. The structure of the proposed CNN is illustrated in Fig. 5.

First, 32 convolutional kernels of size 7×7 are employed to extract low-dimensional feature maps from the input phase images containing noise. Subsequently, the feature maps are fed into 19 Dilation Convolutional Residual Modules to extract high-dimensional feature maps. This module consists of a residual structure composed of two convolutional layers with kernel sizes of 3×3, enhancing the stability and convergence speed of CNN training. The first layer uses a regular convolutional kernel, and the second layer uses a dilation convolutional kernel to enhance the receptive field and feature extraction capability of CNN. The LeakyReLU is used as activation function for each convolutional layer. The low-dimensional and high-dimensional feature maps are fed into the subspace attention [27], [28] module for noise separation. Two convolutional layers with kernel sizes of 3×3 and 1×1 are further used to generate the noise phase map. At last, by subtracting the noise phase map (φ_{noise}) from the original input phase map (φ), the denoised sample phase map (φ_{sample}) can be obtained.

The simulated dataset is generated according to (3). In order to simulate different sample structures, in an image matrix of 512 pixels in both width and height, 8 to 64 rectangles are randomly filled with 1, and the overlapping regions and regions without rectangle are filled with 0. This image matrix is then multiplied by a random value in the range of 0 to π to simulate the height of sample. Thus, the sample phase maps can be obtained. For the noise phase maps generated by Perlin noise model, the mean values are set as 0 rad and the standard deviation (STD) values are in the range of 0.05 to 0.26 rad based on experimental statistics. Finally, the noise phase is added to the sample phase to obtain the input data for training the CNN. In the training stage of CNN, the learning rate is initially set to 0.0001 and its decreasing strategy is cosine annealing function, and the root mean square error (RMSE) is chosen as the loss function. The network weights are optimized using Adam optimization algorithm with parameters of $\beta_1 = 0.9$, $\beta_2 = 0.999$, and $\epsilon = 10^{-8}$. The training process takes 40 000 pairs of data and performs 20 iterations.

III. Simulation Evaluation

To validate the denoising effectiveness of the proposed CNN trained on the Perlin dataset for DHHPN, two simulation experiments were implemented. In the first experiment, the denoising performances of different noise models for DHHPN reduction were compared. First, a simulated ideal sample phase is generated as shown in Fig. 6(g1). It includes some cylindrical and rectangular steps with a height of 2 rad, and the phase of background region is set to 0 rad. By adding the DHHPN shown in Fig. 2(f1) to this sample phase map, an original phase map containing noise is obtained, as shown in Fig. 6(a1). Then, other four datasets corresponding to the noise models of Uniform, Normal, Pink, and Brown were generated using the same routine as the Perlin noise dataset mentioned above. The CNN was trained on those four datasets and Perlin noise dataset, respectively, and performed denoising on Fig. 6(a1) in turn. The output results of CNN are shown in Fig. 6(b1)–(f1) and their corresponding 3-D phase distributions are shown in Fig. 6(b2)–(f2). It can be seen that, the denoising performances of the CNN trained on

TABLE I
SCALABILITY OF THE PROPOSED CNN AT DIFFERENT NOISE LEVELS

Groups	Noise STD (rad)	PSNR (dB)		SSIM (%)	
		Original	Proposed	Original	Proposed
1	0.05	21.85	30.07	87.11	96.31
2	0.10	17.21	30.41	74.19	95.84
3	0.20	13.89	31.49	55.73	95.74
4	0.30	11.87	26.99	46.78	94.26
5	0.40	11.09	19.71	39.78	62.59

datasets of Uniform, Normal, and Pink are poor. On the contrary, the denoising performances of the CNN trained on datasets of Brown and Perlin are much better. In Fig. 6(b1)–(f1), the STD values of two different background regions are calculated to quantitively evaluate the denoising performance. Obviously, the denoising result of CNN trained on Perlin dataset has the best performance with smallest STD values of 0.006 rad for horizontal line and 0.005 rad for vertical line. Furthermore, comparing with the ideal sample phase shown in Fig. 6(g1), the peak signal-to-noise ratio (PSNR), structural similarity (SSIM), and mean absolute error (MAE) of Fig. 6(a1)–(f1) are also calculated by (4), (5), and (6), respectively, and their results are shown in Fig. 6(h). The PSNR, SSIM, and MAE isgiven, respectively, by

$$\mathrm{PSNR} = 10 \cdot \log_{10}\left(\frac{\mathrm{MAX}_I^2}{\mathrm{MSE}(\varphi_r, \varphi_f)}\right) \tag{4}$$

$$\mathrm{SSIM}(f, r) = \frac{(2\mu_f\mu_r + C_1)(2\sigma_{fr} + C_2)}{(\mu_f^2 + \mu_r^2 + C_1)(\sigma_f^2 + \sigma_r^2 + C_2)} \tag{5}$$

$$\mathrm{MAE} = \frac{1}{mn}\sum_{i=1}^{m}\sum_{j=1}^{n}|\varphi_f(i,j) - \varphi_r(i,j)| \tag{6}$$

where MAX_I is the maximum pixel value of the phase map, MSE stands for mean squared error, and φ_f and φ_r denote the filtered phase map and the reference phase map, respectively. The local mean, standard deviation, and cross covariance of phase map φ_f and φ_r are denoted as μ_f, μ_r, σ_f, σ_r, and σ_{fr}, respectively. C_1 and C_2 are constants. It can be seen that, before denoising, the original phase map has the lowest PSNR and SSIM, which are 15.3 dB and 68.0%, respectively. After denoising using CNN trained on different datasets, both PSNR and SSIM are improved. Obviously, the denoising result of CNN trained on Perlin dataset has the highest PSNR and SSIM, which are 28.6 dB and 95.6%, respectively, and the lowest MAE, which is 3.5×10^{-2} rad. Therefore, these experimental results indicate that the CNN trained on the Perlin dataset performs best in reducing the DHHPN.

In the second experiment, denoising performances of phase maps with different Perlin noise levels were evaluated. First, as shown in Table I, five different Perlin noise phase maps with mean values being 0 rad and STD values, respectively, being 0.05 rad, 0.10 rad, 0.20 rad, 0.30 rad, and 0.40 rad are added to the simulated sample phase map shown in Fig. 6(g1). Then, the original phase maps of each group are denoised using the proposed CNN trained on the Perlin dataset. For quantitative evaluation, the PSNR and SSIM of the phase maps before and after denoising are compared. From groups 1 to 3 in Table I, When the noise level falls within the range of the noise level of the training dataset, the denoising performances are very convincing, with PSNR higher than 30.07 dB and SSIM higher than 95.74%. Surprisingly, for group 4 in Table I with initial noise level exceeding that of training dataset (maximum of 0.26 rad), its denoising result is also acceptable, with PSNR and SSIM being greatly improved from 11.87 to 26.99 dB and 46.78% to 94.26%, respectively. From group 5 in Table I, where the noise level increases to nearly twice the maximum noise level in the training dataset, the denoising performance significantly decreases but not completely fails, with PSNR and SSIM being improved only from 11.09 to 19.71 dB and from 39.78% to 62.59%. These results demonstrated the proposed CNN has good scalability for different noise levels.

IV. EXPERIMENTAL MEASUREMENT RESULTS

To evaluate the practical denoising performance of the proposed CNN based on Perlin noise similarity, a standard microstructure with a nominal step height of 65 nm and a MEMS chip were measured in the experiment. A reflective off-axis DHM optical setup using He-Ne laser (wavelength $\lambda = 633$ nm) as illuminating light was constructed to record the holograms of two samples. By implementing +1 term spectrum extraction, angular spectral diffraction, phase unwrapping [29], and phase aberration compensation, the continuous phase maps φ containing DHHPN can be obtained. Then, the images and profiles of the samples before and after denoising can be calculated according to $h = \varphi\lambda/4\pi$ or $h = \varphi_{\text{sample}}\lambda/4\pi$. The unfiltered (Original) measurement results of microstructure and MEMS chip and their corresponding results after denoising using WFF-BM3D [30], DnCNN trained on Perlin dataset, and the proposed method are shown in Fig. 7. Similarly, the STD values of the background and structure regions labeled with white curves in Fig. 7(a1)–(d1) and (a3)–(d3) are calculated to quantitively evaluate the denoising performances of different methods. As summarized in Table II, for the two samples, the average values of the STD values of two regions before denoising are 4.64 nm and 5.27 nm, respectively. After applying the WFF-BM3D algorithm, the noise of the two samples are partially suppressed, with average STD values of 3.37 nm and 2.20 nm, respectively. After performing DnCNN denoising, the noise suppression effects in different regions are quite different. The noise suppression performance is quite good in the background region and a slight poor in the sample region, with average STD values of 1.80 nm and 2.30 nm, respectively. Inspiring, the overall noise suppression performance of the proposed method far exceeds the other two methods. The denoising performance in the background and sample areas is highly consistent, with the STD values in both areas reduced by an order of magnitude to 0.22 nm and 0.38 nm, respectively. In addition, these experimental results are in good agreement with the simulation results shown in Fig. 6(f1), where 0.006 rad corresponds to 0.30 nm.

To evaluate the actual measurement accuracy, the profile curves along the red dashed lines obtained by Original, WFF-BM3D, DnCNN, and the proposed method were compared with the results measured using a white light interferometer

TABLE II
EXPERIMENTAL EVALUATION OF DENOISING PERFORMANCE FOR DIFFERENT METHODS

Methods	Standard microstructure				MEMS chip			
	STD (nm)			Time (s)	STD (nm)			Time (s)
	Background	Sample	Average values		Background	Sample	Average values	
Original	3.82	5.46	4.64	–	5.04	5.51	5.27	–
WFF-BM3D	2.23	4.50	3.37	23.72	2.64	1.75	2.20	18.18
DnCNN	0.19	3.42	1.80	1.40	0.14	4.46	2.30	1.09
Proposed	0.11	0.34	0.22	1.75	0.32	0.44	0.38	1.23

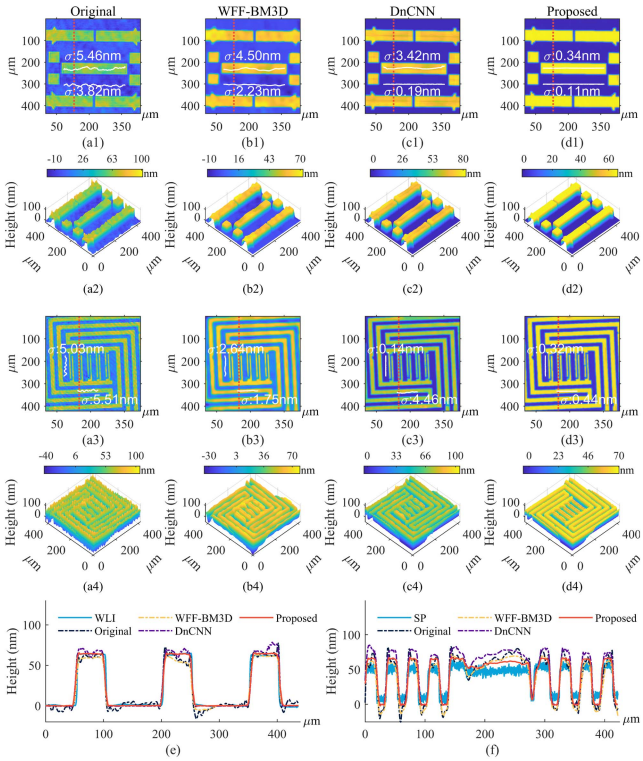

Fig. 7. Measurement results of the standard microstructure and MEMS chip. (a1)–(a4) Original 2-D images of the samples and their corresponding 3-D distributions. (b1)–(b4) Denoising results obtained using the WFF-BM3D algorithm. (c1)–(c4) Denoising results obtained using the DnCNN trained on Perlin dataset. (d1)–(d4) Denoising results obtained using the proposed method. (e) Profiles of red dashed lines in (a1)–(d1) and measurement profile obtained using WLI. (f) Profiles of red dashed lines in (a3)–(d3) and measurement profile obtained using SP.

(WLI) (Zygo, NewView 9000) and using a stylus profilometer (SP) (S1910DX3; ACCRETECH), respectively. As shown in Fig. 7(e) and (f), for the Original and WFF-BM3D results, the height errors in both the background and sample areas ranged from several to tens of nanometers, especially at the edges of structures. For the DnCNN results, the background area is relatively flat, but the sample area is less ideal, showing differences of tens of nanometers compared to the measurements obtained using WLI and SP. The results of the proposed method exhibited a very flat background area, and the height values in the sample area were more consistent with those of WLI and SP. In addition, when training DnCNN with the Perlin dataset, the network's loss function only converged to 0.04, and the training process exhibited instability. In contrast, training the proposed CNN achieved a lower loss function convergence of 0.01. Therefore, the proposed CNN has higher fitting accuracy, and the training process is more stable.

In addition, as shown in Table II, despite having a more complex network structure than the DnCNN, the time consumption of the proposed method is still very close to DnCNN and much shorter than WFF-BM3D. Therefore, the proposed CNN based on Perlin noise similarity has a significant potential for denoising DHHPN in DHM experiment. All data processing was performed on a Dell PC running Windows 10 operating system, with an Intel(R) Xeon(R) Gold 5118 CPU @2.30 GHz processor.

V. CONCLUSION

In summary, accurate representation of actual DHHPN is the key prerequisite to realize phase denoising and improve measurement accuracy. We experimentally demonstrated a continuous phase denoising via deep learning based on Perlin noise similarity. First, Fourier spectra and the autocorrelation functions of background region in a continuous phase map obtained from DHM experiment and UNPBP noises were analyzed and compared, and their correlations were calculated. To the best of our knowledge, the characteristic similarity between DHHPN and Perlin noise was revealed for the first time in this paper. Second, the noise features of other six phase maps obtained with different illumination light, different DH/DHM systems, and different samples were studied, which further verified the characteristic similarity between DHHPN and Perlin noise. Then, inspired by this discovery, Perlin noise was used to simulate the real DHHPN. And the CNN was trained using a dataset consisting only of computationally generated clean sample phase maps and Perlin noise phase maps. This not only solves the problems of collecting and labeling experimental data, but also improves the universality of the trained CNN model for different DH/DHM systems. Simulation and experimental results validated that: 1) compared with other noise models, the CNN trained using dataset generated by Perlin noise model has the best denoising performance for DHHPN, with STD values of phase in the background regions achieving 0.005 rad and 0.006 rad, respectively; 2) the proposed CNN has good scalability for different noise levels; and 3) the denoising performance of the proposed method is superior to classical algorithms, where the measurement accuracy of standard microstructure and MEMS

chip are improved by an order of magnitude, with average values of STD achieving 0.22 nm and 0.38 nm.

The primary aim of this article is to address the challenge of hybrid noise affecting the accuracy in digital holographic microstructure measurement. The task involves not only effectively suppresses noise, but also maintains the inherent structure of the sample. This work strikes a balance between these two objectives. It should be noted that if the sample phase distribution exhibits characteristics similar to Perlin noise, such as some biological tissues and cells, the sample profiles may be excessively smoothed. Therefore, the proposed method is more suitable for samples with distinct structures or step-like distributions. In addition, the parameters of Perlin need guidance from a small amount of experimental statistical data, such as means, standard deviation values, and spectral ranges. When the statistical estimation of noise parameters in the experiment is inaccurate or there are too many outliers, the Perlin noise will fail to accurately simulate real DH noise.

REFERENCES

[1] V. Bianco et al., "Strategies for reducing speckle noise in digital holography," *Light Sci. Appl.*, vol. 7, no. 1, 2018, Art. no. 48.

[2] Z. Lin et al., "Digital holographic microscopy phase noise reduction based on an over-complete chunked discrete cosine transform sparse dictionary," *Opt. Lasers Eng.*, vol. 166, Jul. 2023, Art. no. 107571.

[3] H. Yu, S. Jia, Y. Liu, and J. Dong, "Phase coherent noise reduction in digital holographic microscopy based on adaptive total variation," *Opt. Lasers Eng.*, vol. 134, Nov. 2020, Art. no. 106204.

[4] K. Dabov, A. Foi, V. Katkovnik, and K. Egiazarian, "Image denoising with block-matching and 3D filtering," in *Proc. SPIE Conf. Image Process.: Algorithms Syst., Neural Netw., Mach. Learn.*, 2006, vol. 6064, pp. 354–365.

[5] J. Zhang, L. Huang, B. Chen, and L. Yan, "Accurate extraction of the +1 term spectrum with spurious spectrum elimination in off-axis digital holography," *Opt. Exp.*, vol. 30, no. 15, pp. 28142–28157, 2022.

[6] Q. Kemao, "Two-dimensional windowed fourier transform for fringe pattern analysis: Principles, applications and implementations," *Opt. Lasers Eng.*, vol. 45, no. 2, pp. 304–317, 2007.

[7] J.-L. Starck, E. J. Candès, and D. L. Donoho, "The curvelet transform for image denoising," *IEEE Trans. Image Process.*, vol. 11, no. 6, pp. 670–684, Jun. 2002.

[8] K. Dabov, A. Foi, V. Katkovnik, and K. Egiazarian, "Image denoising by sparse 3-D transform-domain collaborative filtering," *IEEE Trans. Image Process.*, vol. 16, no. 8, pp. 2080–2095, Aug. 2007.

[9] S. Montresor, M. Tahon, A. Laurent, and P. Picart, "Computational denoising based on deep learning for phase data in digital holographic interferometry," *APL Photon.*, vol. 5, no. 3, 2020, Art. no. 030802.

[10] K. Yan, Y. Yu, T. Sun, A. Asundi, and Q. Kemao, "Wrapped phase denoising using convolutional neural networks," *Opt. Lasers Eng.*, vol. 128, 2020, Art. no. 105999.

[11] B. Lin, S. Fu, C. Zhang, F. Wang, and Y. Li, "Optical fringe patterns filtering based on multi-stage convolution neural network," *Opt. Lasers Eng.*, vol. 126, 2020, Art. no. 105853.

[12] D. Yin et al., "Speckle noise reduction in coherent imaging based on deep learning without clean data," *Opt. Lasers Eng.*, vol. 133, Oct. 2020, Art. no. 106151.

[13] Q. Fang et al., "Speckle denoising based on deep learning via a conditional generative adversarial network in digital holographic interferometry," *Opt. Exp.*, vol. 30, no. 12, pp. 20666–20683, 2022.

[14] W. Jeon, W. Jeong, K. Son, and H. Yang, "Speckle noise reduction for digital holographic images using multi-scale convolutional neural networks," *Opt. Lett.*, vol. 43, no. 17, pp. 4240–4243, 2018.

[15] J. Wu, J. Tang, J. Zhang, and J. Di, "Coherent noise suppression in digital holographic microscopy based on label-free deep learning," *Front. Phys.*, vol. 10, 2022, Art. no. 880403.

[16] M. Tahon, S. Montresor, and P. Picart, "Towards reduced CNNs for denoising phase images corrupted with speckle noise," *Photonics*, vol. 8, no. 7, Jul. 2021, Art. no. 255.

[17] K. Yan, Y. Yu, C. Huang, L. Sui, K. Qian, and A. Asundi, "Fringe pattern denoising based on deep learning," *Opt. Commun.*, vol. 437, pp. 148–152, 2019.

[18] C. Zuo et al., "Deep learning in optical metrology: A review," *Light Sci. Appl.*, vol. 11, no. 1, 2022, Art. no. 39.

[19] K. Zhang, W. Zuo, Y. Chen, D. Meng, and L. Zhang, "Beyond a Gaussian denoiser: Residual learning of deep CNN for image denoising," *IEEE Trans. Image Process.*, vol. 26, no. 7, pp. 3142–3155, Jul. 2017.

[20] S. Montrésor and P. Picart, "On the assessment of de-noising algorithms in digital holographic interferometry and related approaches," *Appl. Phys. B*, vol. 128, no. 3, Mar. 2022, Art. no. 59.

[21] M.-L. Cruz and K. G. González-Velázquez, "Analysis of random-phase distributions and Perlin noise in CGH: A study of its effects on Fourier and Fresnel holograms reconstruction," *Opt. Eng.*, vol. 59, no. 10, pp. 102419–102419, 2020.

[22] K. Marcin, "N-dimensional 1/beta (e.g. pink, brown, blue) noise generation via spectral shaping of white noise," GitHub, 2019. [Online]. Available: https://github.com/MarcinKonowalczyk/randnd

[23] A. Biagioli, "Understanding perlin noise," adrian's soapbox, Aug. 2014. [Online]. Available: https://adrianb.io/2014/08/09/perlinnoise

[24] M. N. Nounou, B. R. Bakshi, and B. Walczak, *Multiscale Methods for Denoising and Compression*. Amsterdam, The Netherlands: Elsevier, 2000.

[25] M. M. Mukaka, "A guide to appropriate use of correlation coefficient in medical research," *Malawi Med. J.*, vol. 24, no. 3, pp. 69–71, 2012.

[26] D. N. Reshef et al., "Detecting novel associations in large data sets," *Science*, vol. 334, no. 6062, pp. 1518–1524, Dec. 2011.

[27] S. Cheng, Y. Wang, H. Huang, D. Liu, H. Fan, and S. Liu, "NBNet: Noise basis learning for image denoising with subspace projection," in *Proc. IEEE/CVF Conf. Comput. Vis. Pattern Recognit.*, 2021, pp. 4896–4906.

[28] C. D. Meyer and I. Stewart, *Matrix Analysis and Applied Linear Algebra*. Philadelphia, PA, USA: SIAM, 2023.

[29] H. Xia et al., "Phase calibration unwrapping algorithm for phase data corrupted by strong decorrelation speckle noise," *Opt. Exp.*, vol. 24, no. 25, pp. 28713–28730, 2016.

[30] M. Zhao and K. Qian, "WFF-BM3D: A hybrid denoising scheme for fringe patterns," in *Proc. Int. Conf. Opt. Photon. Eng.*, 2015, vol. 9524, pp. 564–569.

Jianjun Tang received the B.E. degree, in 2018, in mechatronics engineering from Zhejiang Sci-Tech University, Hangzhou, China, where he is currently working toward the Ph.D. degree in mechanical engineering with the School of Mechanical Engineering, since 2020.

His research interests include machine learning, deep learning, image processing, computer vision, and data analysis.

Benyong Chen received the M.E. and Ph.D. degrees in mechanical engineering from Zhejiang University, Hangzhou, China, in 1992 and 2000, respectively.

From 2000 to 2002, he was a Postdoctoral Researcher in optical engineering with Tsinghua University, Beijing, China. He is currently a Professor and Ph.D. Supervisor of mechanical engineering with the School of Information Science and Engineering, Zhejiang Sci-Tech University, Hangzhou, China. He has authored or coauthored more than 100 papers in his research career. His research interests include nanometer displacement measurement and instruments, microactuators, precision measurement, and control technology.

Dr. Chen was the recipient of the National Invention 2nd Prize of China, in 2007.

Liping Yan received the M.E. degree in electrical engineering from Chongqing University, Chongqing, China, in 2003, and the Ph.D. degree in mechanical manufacture and automation from Zhejiang Sci-Tech University, Hangzhou, China, in 2014.

She is currently a Professor and Ph.D. Supervisor of mechanical engineering with the School of Information Science and Engineering, Zhejiang Sci-Tech University. She has authored and coauthored more than 80 papers. Her current research interests include laser interferometric displacement/absolute distance measurement, digital holographic imaging, and photoelectric signal processing.

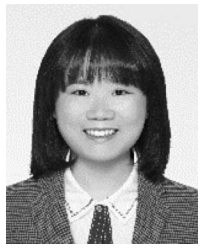

Liu Huang received the M.E. degree in measurement and testing technologies and instruments from China Jiliang University, Hangzhou, China, in 2012, and the Ph.D. degree in mechanical engineering from Zhejiang Sci-Tech University, Hangzhou, China, in 2021.

She is currently a Lecturer with Zhejiang Sci-Tech University, since 2021. Her current research interests include digital holographic imaging and 3-D morphology measurement of microstructures.